

Topological phases of monolayer and bilayer depleted Lieb lattices

Arghya Sil^{1,*} and Asim Kumar Ghosh^{1,†}

¹*Department of Physics, Jadavpur University, 188 Raja Subodh Chandra Mallik Road, Kolkata 700032, India*

Existence of nontrivial topological phases in a tight binding Haldane-like model on the depleted Lieb lattice is reported. This two-band model is formulated by considering the nearest-neighbor, next-nearest-neighbor and next-next-nearest-neighbor hopping terms along with complex phase which breaks the time reversal symmetry of this semi-metallic system. Topological feature of this model is studied along with the presence of sublattice symmetry breaking staggered onsite energy. Combined effect of these two broken symmetries is found crucial for an additional transition between nontrivial and trivial phases. System exhibits two types of phase transitions, say, between two nontrivial phases and nontrivial to trivial phases. Nonzero Chern numbers, existence of Hall plateau and symmetry protected edge states confirm the presence of the nontrivial phases. This two-band system hosts four different types of phases where two are topological. Additionally topological properties of stacked bilayer of the depleted Lieb lattices is also studied with similar Haldane-like Hamiltonian. This four-band system is found to host Chern insulating phases, with higher values of Chern numbers supported by in-gap edge states.

Corresponding author: Asim Kumar Ghosh

PACS numbers:

I. INTRODUCTION

Discovery of topological insulator (TI) has triggered a plethora of research activity in order to find this bulk insulating phase within a variety new systems. It began with the finding of Quantum Hall Effect (QHE) by K Von Klitzing¹ where strong magnetic field quantized the Hall conductivity of two-dimensional (2D) electron gas and the topological phase was characterized by Thouless-Kohmoto-Nightingale-Nijs (TKNN) invariant². In another breakthrough, F D M Haldane discovered quantum anomalous Hall effect (QAHE), where quantization of Hall Conductivity was found even in the absence of true magnetic field, but in the presence of complex hopping terms, which breaks the time reversal symmetry (TRS)³. In this investigation, Haldane formulated a tight-binding model on the honeycomb lattice where the next-nearest-neighbor (NNN) hopping parameters pick up additional phase which essentially induces this novel insulating phase.

For 2D systems, this class of insulating phase is characterized by nonzero values of topological invariant known as Chern number (C). Systems only with multiple bulk bands could host this particular phase, where several bands assume definite values of C . In addition the system hosts topological edge states in this phase, where the number of such states is determined by the value of C which is governed by the bulk-boundary correspondence rule⁴. Order of TIs can be defined in terms of the rule which states that n -th order TI in d spatial dimension gives rise to symmetry protected states at $(d - n)$ dimension where n is an integer⁵⁻⁷. For the Chern insulating (CI) phase $d = 2$, and $n = 1$. Experimental realization of Haldane phase have been made possible by optical lattices of ultracold atoms^{8,9}.

Investigations are continued afterwards by formu-

lating Haldane-like tight binding models beyond the honeycomb lattice in order to find this novel phase in a series of subsequent studies. As a result, this insulating phase is observed in other 2D lattices, for examples in α - \mathcal{T}_3 ¹⁰, dice¹¹, Lieb¹², kagome^{13,14}, stuffed honeycomb¹⁵, checkerboard¹⁶, star^{17,18}, square-octagon^{13,19} lattices etc. Side by side, many different classes of TIs have been discovered, and classified. For example, spin-orbit coupling induced TRS-protected TIs are characterized by Z_2 invariant²⁰. Different kind of insulating phases are introduced depending on the perturbation on the system. For example, in Floquet topological insulators (FTI), the system hosts topological phase under photo-irradiation which is otherwise trivial^{21,22}. In another series of studies, nontrivial topological phase is found in bosonic magnon excitations which are identified as topological magnon insulator (TMI)^{7,23}. This particular phase is observed in ferromagnetic (FM) Kitaev-Heisenberg models in the presence of external magnetic field formulated on honeycomb lattice with spin-anisotropic interaction and on CaVO lattice with Dzyaloshinskii-Moriya (DM) interactions^{24,25}. The bosonic magnon dispersion is found topological for both the cases. FM Heisenberg model on breathing kagome lattice hosts first as well as second order topological phases⁷. Existence of topological phases is further observed in antiferromagnetic (AFM) Heisenberg models formulated on honeycomb and CaVO lattices^{26,27}. However, in these models, bosonic triplet excitation on hexagonal and square plaquettes is found topological for the respective lattices. These are few of the examples in the vast domain of different types of TI's.

In order to frame multi-band systems with single atomic orbital, topological models are generally formulated on the non-Bravais lattices. From the structural

point of view, those lattices can be divided into two different groups. Based on their origin, all those 2D lattices are derived eventually from either square or triangular lattices which are Bravais. For examples, Lieb¹², CaVO^{25,27,28}, square-octagon^{13,19} and checkerboard¹⁶ lattices belong to first group as they are derived from square lattice either by depleting lattice sites or introducing nonsymmetric hopping terms in the Hamiltonian. However, their reciprocal lattice is always a square lattice. More precisely, Lieb, CaVO and square-octagon lattices are nothing but depleted square lattice, where 25% of sites are removed from the square lattice in a regular manner for the Lieb lattice. For both CaVO and square-octagon lattices, 20% of the sites are removed. On the other hand, checkerboard lattice is nothing but (undepleted) square lattice where tight-binding Hamiltonian is formulated by invoking nonsymmetric hopping terms. Finally, symmetry of the resulting Hamiltonian depends on the nature of depletion and arrangement of hopping paths.

In the same way, honeycomb³, stuffed-honeycomb¹⁵, kagome^{13,14}, breathing kagome⁷, star^{17,18}, α - \mathcal{T}_3 ¹⁰ and dice¹¹ lattices constitute the second group as they are derived from the triangular lattice. So their reciprocal lattice is also triangular. In this group, honeycomb, kagome, breathing kagome and star lattices are depleted triangular lattice while stuffed-honeycomb, α - \mathcal{T}_3 and dice lattices are essentially triangular lattice with nonsymmetric hopping bonds. Both of them are tripartite also. In this study, Haldane-like model is formulated on the depleted Lieb lattice which is found capable to host nontrivial topological phases. This depleted Lieb lattice is constructed from the square lattice by erasing 50% of its sites. Lieb lattice is tripartite square lattice while the depleted one is bipartite.

On the other hand, a number of investigations have been parallelly carried out on the Haldane model formulated over bilayer systems those yield nontrivial phases, specially on bilayer graphene systems²⁹. Topological characterization of such systems facilitates the emergence of new phases in the expanded parameter space where the band structure gets enriched due to the multiplication of band number by two. In another study, existence of flat bands with nonzero Chern number and fractional QHE has been reported on twisted bilayer graphene³⁰. In this work, a Haldane model on the bilayer depleted Lieb lattice has also been formulated where a pair of topological phases is found to exist.

Among those several lattice systems exhibiting CI phase as pointed out above, the most fascinating one is the Lieb lattice since it exhibits several exotic topological properties under various interactions as summarized here. Tight-binding and Heisenberg models formulated on Lieb lattice essentially yield a three-band systems as it is composed of three non-equivalent lattice sites. In tight-binding regime, it shows a flat band³¹ and a quadratic band crossing point or a Dirac cone, which is found topologically protected. In the presence of spin-orbit coupling (SOC) or incorporation of complex NNN hopping term, a gap opens up at the

Dirac point and the model becomes topological^{32,33}. Since the Lieb lattice possesses inversion symmetry this phase is characterized by Z_2 topological invariant¹². FTI phase on Lieb lattice has also been reported in helical photonic wave-guide³⁴. TMI phase is found in FM Heisenberg model framed on Lieb lattice along with DM interaction³⁵. Stacked multi-layer Lieb lattices have been shown to host CI phase with high Chern numbers in the presence of SOC³⁶. Basically Lieb lattice is the 2D analogue of the 3D lattice found in perovskites. There have been several efforts to realize materials based on the Lieb lattice. This 2D structure has been successfully demonstrated by means of photonic and cold-atom crystals. In another attempt, it has been synthesized by the surface state electrons of Cu(111) confined by an array of CO molecules positioned with a scanning tunnelling microscope³⁷. More recently, first principle study predicts that two covalent organic frameworks, sp^2 C-COF and sp^2 N-COF are actually two material realizations of organic-ligand-based Lieb lattice³⁸.

Depleted Lieb lattice was introduced before by Oliveira *et. al.*, where a XXZ Heisenberg model was formulated on this lattice. The magnetic model comprised of three different nearest-neighbor FM exchange interactions³⁹. However, no topological phase was found even in the presence of DM and external magnetic field. In this work, we focus on the depleted Lieb lattice, and its bilayer structure. But nontrivial topological phases are obtained by formulating tight-binding Hamiltonian on those systems. This lattice is constructed from the Lieb lattice by removing few lattice sites in a regular way. A closer look reveals that it is nothing but the Bravais lattice with rectangular unit cell. And this particular geometry is formed by the Cu atoms observed in doped cuprate superconductors with larger Cu-O-Cu bond length and smaller buckling degree⁴⁰. However, a tight-binding model similar to the Haldane model with nonsymmetric terms is formulated in such a way that the resulting system can be studied in terms of non-Bravais depleted Lieb lattice. In this model next-next-nearest-neighbour (NNNN) hopping terms are made complex unlike the original Haldane model where NNN terms are complex instead³. Without the NNNN hopping the system is again trivial although the presence of staggered site energy induce a gap in this two-sublattice system. Both the complex NNNN hopping and staggered onsite energy are the essential ingredients of this model. The effect of uniform onsite energy would be trivial for obvious reasons.

Furthermore, a coupled bilayer version of this depleted Lieb lattice is introduced where the coupling among the layers is accomplished by the inter-layer hopping between same type of nearest-neighbor (NN) sublattice sites. It is shown that the bilayer system hosts four different topological phases. It is expected that those depleted lattice structures can be generated using the same techniques employed for Lieb lattice as discussed before³⁷.

The article is organized in the following way. In section II, depleted Lieb lattice is described and the

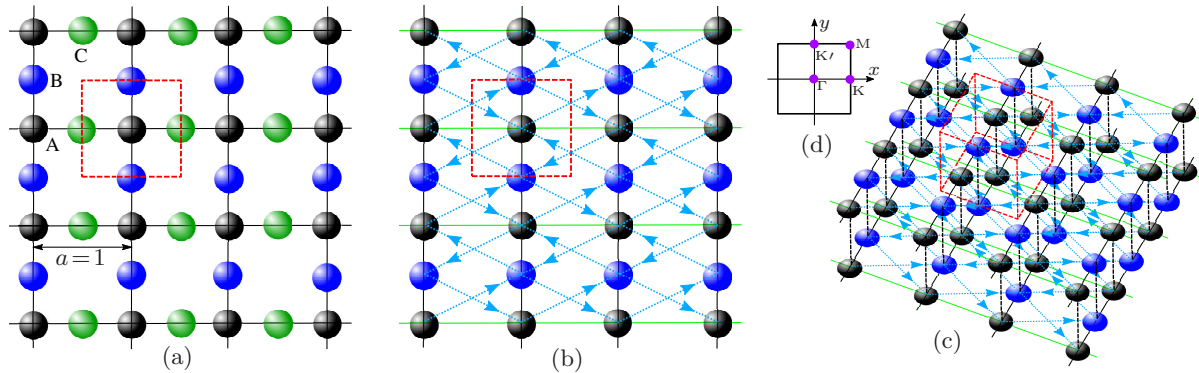


FIG. 1: (a) Lieb lattice with three basis points shown by black (A), blue (B) and green (C) spheres. Unit cell is shown by red dashed square. (b) Depleted Lieb lattice with two basis points shown by black (A), blue (B). Strength of NN hopping between A and B sites along y direction is t_1 (black line). Strength of NNN hopping between A sites along x direction is t_2 (green line), while t_3 is that along the diagonals between the NNNN lattice sites (blue dotted line). Sign of the complex phase is assumed positive when hopping is along the direction of the arrow. (c) Bilayer depleted Lieb lattice, where the hopping strength between top and bottom layers is t_4 (black dashed line). (d) The first Brillouin zone (BZ) of the lattice. High-symmetry points of square BZ, Γ (0, 0), K (π , 0), K' (0, π), and M (π , π) have been marked.

tight-binding Hamiltonian is formulated. In section III, spectral properties are described. This is followed by section IV, where the topological phases of this monolayer system are presented. In next section V, topological properties of the bilayer version of this lattice are described. Finally, in section VI, discussions and conclusions on this work are summarized.

II. FORMULATION OF TIGHT-BINDING HAMILTONIAN ON DEPLETED LIEB LATTICE

Geometry of 2D Lieb lattice consisting of three sublattices with A (black), B (blue) and C (green) spheres is shown in Fig. 1(a). Unit cell is shown by red dashed square containing the three different sites. The depleted Lieb lattice is shown in Fig. 1(b), where the green sub-lattice points are removed. This two-sublattice system can be generated alternatively by depleting blue sub-lattice points instead of green. The resulting structure is nothing but the rectangular Bravais lattice. The NN bonds are depicted in black, while the NNN bonds are green. The NNNN hoppings are complex as well as nonsymmetric owing to their directionality. Because of this nonsymmetric bonds the resulting Hamiltonian is composed on this non-Bravais lattice. It means adjacent rectangular plaquettes along the vertical direction are not identical. Although the Lieb lattice preserves the four-fold rotational symmetry (C_4) of the square lattice, depleted Lieb lattice possesses the two-fold (C_2) rotational symmetry. Now, the tight-binding Hamiltonian on this system is formulated as

$$H = \left[t_1 \sum_{\langle jj' \rangle} c_j^\dagger c_{j'} + t_2 \sum_{\langle\langle jj' \rangle\rangle \in A} c_j^\dagger c_{j'} + t_3 \sum_{\langle\langle\langle jj' \rangle\rangle\rangle} e^{i\phi_{jj'}} c_j^\dagger c_{j'} + H.c. \right] + \sum_j \mu_j c_j^\dagger c_j. \quad (1)$$

The summations $\langle \cdot \rangle$, $\langle\langle \cdot \rangle\rangle$ and $\langle\langle\langle \cdot \rangle\rangle\rangle$ run over NN, NNN and NNNN pairs, respectively. c_j^\dagger (c_j) is the fermionic creation (annihilation) operator for an electron at the j -th site. t_1 , t_2 and t_3 is the strength of NN, NNN and NNNN hopping, those are shown in black, green lines and blue dotted arrow, respectively in Fig. 1(b). μ_j is the site dependent chemical potential. The direction of the phases $\phi_{jj'}$ is shown in Fig 1 (b). The sign of $\phi_{jj'}$ is assumed positive, $\phi_{jj'} = \phi$ (negative, $\phi_{jj'} = -\phi$), when it is directed along (opposite) the arrowhead. Sign of the phases are chosen in this way to ensure the net effective magnetic field arising from those phases per square plaquette is zero. The onsite energy is taken as $\mu = -\mu_A = \mu_B$, which breaks sublattice symmetry. Hamiltonian can be expressed as

$$H = \sum_{jj'} \psi_j^\dagger g_{jj'} \psi_{j'}, \quad (2)$$

where $\psi_j^\dagger = [c_{A_j}^\dagger \ c_{B_j}^\dagger]$, $g_{jj'} = g_0 I_0 + \mathbf{g} \cdot \boldsymbol{\sigma}$, $g_0 = t_2 \delta_{j,j' \in A}$, $g_x = t_1 \delta_{j,j' \in NN} + t_3 \cos(\phi) \delta_{j,j' \in NNNN}$, $g_y = t_3 \sin(\phi) \delta_{j,j' \in NNNN}$, $g_z = -\mu$, I_0 is the 2×2 identity matrix and σ_α , $\alpha = x, y, z$ are the Pauli matrices.

Length of the each side of the square unit cell is set as the unity ($a = 1$). The NN vectors between A and B sites are $\boldsymbol{\delta}_1 = (0, 1/2)$, the NNN vector between the A sites are $\boldsymbol{\delta}_2 = (1, 0)$ and the NNNN vectors between the A and B sites along the diagonals are $\boldsymbol{\delta}_3 = (1, 1/2)$. We set $t_1 = 1$ throughout the article. Hamiltonian is transformed into the reciprocal space under the Fourier transformation,

$$c_j = \frac{1}{\sqrt{N}} \sum_{\mathbf{k} \in \text{BZ}} c_{\mathbf{k}} e^{i\mathbf{k} \cdot \mathbf{R}_j},$$

where N is the number of unit cells, $\mathbf{k} = (k_x, k_y)$, and \mathbf{R}_j is the Bravais vector for the site j . So the Hamiltonian is

$$H = \sum_{\mathbf{k}} \psi_{\mathbf{k}}^\dagger h(\mathbf{k}) \psi_{\mathbf{k}}, \quad (3)$$

where $\psi_{\mathbf{k}}^\dagger = [c_{A\mathbf{k}}^\dagger \ c_{B\mathbf{k}}^\dagger]$, is a two-component spinor and $h(\mathbf{k}) = h_0 I_0 + \mathbf{h} \cdot \boldsymbol{\sigma}$, where,

$$\begin{cases} h_0 = t_2 \cos k_x, \\ h_x = 2t_1 \cos\left(\frac{k_y}{2}\right) + 4t_3 \cos(\phi) \cos(k_x) \cos\left(\frac{k_y}{2}\right), \\ h_y = 4t_3 \sin(\phi) \sin(k_x) \sin\left(\frac{k_y}{2}\right), \\ h_z = t_2 \cos k_x - \mu. \end{cases}$$

The phase ϕ appears here in the off-diagonal terms while it is found in diagonal terms for the Haldane model³. Conservation of TRS and particle-hole symmetry (PHS) for $h(\mathbf{k})$ means that the following relations

$$\begin{cases} \mathcal{T} h(\mathbf{k}) \mathcal{T}^{-1} = h^*(-\mathbf{k}), \\ \mathcal{P} h(\mathbf{k}) \mathcal{P}^{-1} = -h^*(-\mathbf{k}), \end{cases}$$

will be satisfied under the appropriate choice of TRS and PHS operators, \mathcal{T} , and \mathcal{P} , respectively. However, no operator is found to satisfy the above relations due to all the components, h_α , being nonzero and their typical dependence on \mathbf{k} . As a consequence, chiral symmetry is also broken. This 2D system belongs to class A, and hence its topological invariant may assume integral value upon its characterization⁴¹. The spectrum of $h(\mathbf{k})$ does not possess the inversion symmetry around the zero energy because of the absence of PHS. Dispersions of this two-band system is given by

$$E_{\pm}(\mathbf{k}) = h_0 \pm \sqrt{h_x^2 + h_y^2 + h_z^2}.$$

The dispersions within the BZ are shown in Fig. 2 for $t_2/t_1 = 3/4$, $t_3/t_1 = 1/4$, $\phi = \pi/3$, and $\mu/t_1 = 1$. It clearly indicates that inversion symmetry for the spectrum of $h(\mathbf{k})$ around $E = 0$ is lost. A band gap exists for obvious reason. Inversion symmetry for the spectrum will be restored if h_0 becomes independent of \mathbf{k} and $h_z = 0$. The band-structures along the high symmetric pathway for various parameter values are obtained and their properties are described in the next section.

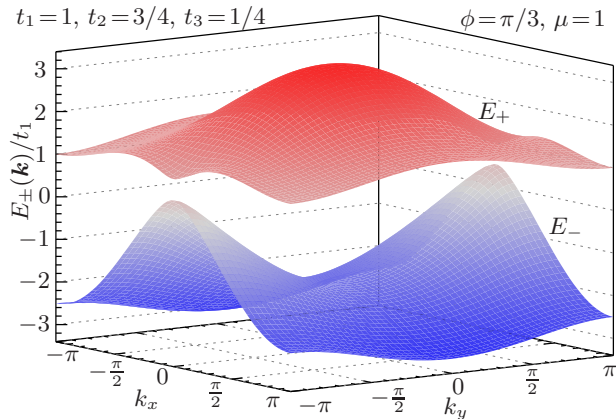


FIG. 2: Dispersion relations, $E_{\pm}(\mathbf{k})$, when $t_2/t_1 = 3/4$, $t_3/t_1 = 1/4$, $\phi = \pi/3$, and $\mu/t_1 = 1$.

III. SPECTRAL PROPERTIES OF DEPLETED LIEB LATTICE

Four different phases of the system are noted, which are shown in six band diagrams in Fig 3(a)-(f). Among them two phases are topological as indicated in Fig 3(b), (e) and (f). In order to explain the character of them, evolution of spectral properties with the variation of complex phase ϕ and onsite energy μ has been demonstrated in this section. So, values of other parameters are kept fixed, namely $t_2/t_1 = 1$ and $t_3/t_1 = 1/2$. When μ and ϕ are both zero, system is defined only by NN, NNN and NNNN interactions. In this condition, the system remains in one of its trivial state, when the two bands touch each other at the point $(k_x, k_y) = (\pi/2, \pi)$, an intermediate between two high symmetry points K' and M , as shown in Fig 3 (a). It means the system always exhibit semimetallic state when $\mu = 0$ and $\phi = 0$. Now, in the presence of complex NNNN phase, $\phi \neq 0$, but $\mu = 0$, the two bands get separated immediately as shown in Fig 3 (b). Again the system remains in semimetallic phase, since the bands are separated by indirect (pseudo) band-gap. This phase is termed as pseudo semimetallic phase. In this case, peak of lower band appears at K' while bottom of upper band remains in M - K region. The system becomes nontrivial as the bands acquire nonzero Chern number. On the other hand, when $\mu \neq 0$, but $\phi = 0$, the band-touching point shifts leftwards with the increase of μ , and at $\mu/t_1 = 1$, it moves ultimately to K' point of the BZ (Fig 3(c)). It happens due to fact that bottom of upper band extends with the increase of μ , and it reaches K' , although peak of lower band remains fixed at K' . This is nothing but another semimetallic phase where band touching occurs at one of the high symmetry points, K' .

With the further increase of μ , or beyond $\mu/t_1 = 1$, but $\phi = 0$, the band gap opens up eventually at the K' point and the system lies in trivial insulating phase. The band-structure at the values of $\mu/t_1 = 1.5$ and $\phi = 0$ is shown in Fig 3(d), which indicates the existence of true band gap. Now, when both the values of μ and ϕ are nonzero, the system is always in a pseudo-gapped phase and in most of the cases, the phase is nontrivial, namely Chern semimetallic (CSM) Phase. One of the case is demonstrated in Fig 3 (e). At these values, both the bands acquire nonzero Chern numbers. The lower (upper) band acquires $C = -1$ ($C = 1$). The sign of the Chern numbers reverses with the sign reversal of ϕ as shown in Fig 3 (f), leading to another CSM phase. The band structures of the last two cases are similar since the magnitudes of all the parameters are the same. However, in every case, it lacks inversion symmetry about $E = 0$, due to obvious reason. Among the four phases, two are topologically nontrivial, while the remaining two are trivial. The trivial phases are insulating and semimetallic. Two CSM phases emerge here, although no CI phase is noted in this case.

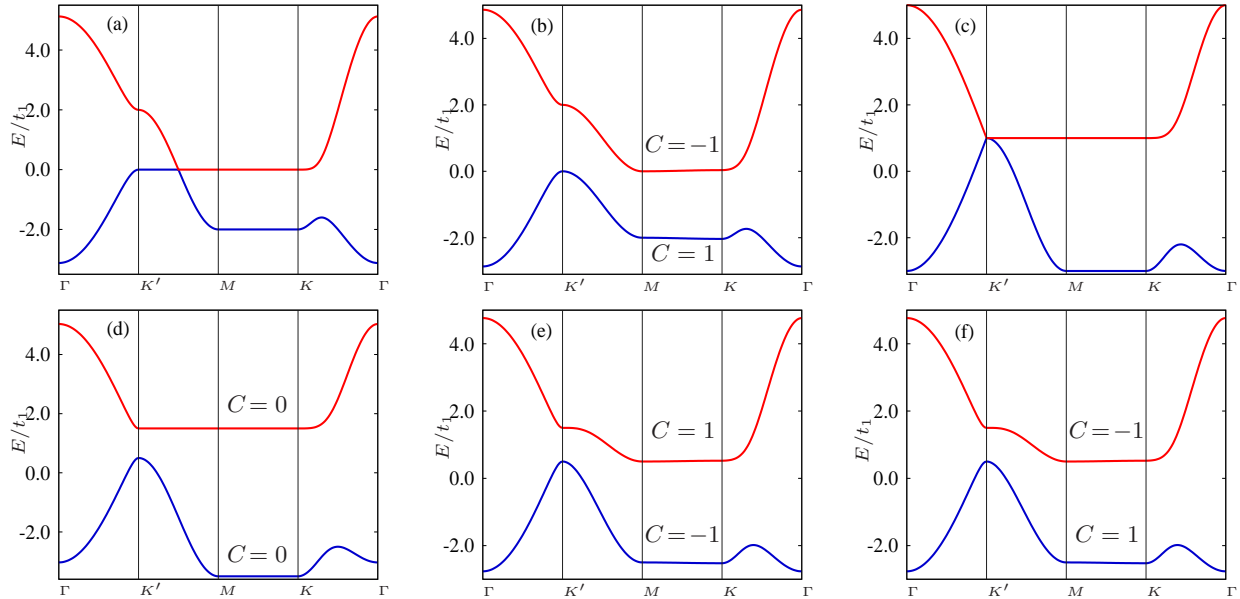


FIG. 3: Band structure of depleted Lieb lattice along the high symmetry pathway Γ - K' - M - K - Γ of the BZ is shown with the variation of μ and ϕ , when $t_2/t_1 = 1, t_3/t_1 = 1/2$. (a) $\mu = 0, \phi = 0$, trivial semi-metallic phase with no band gap, (b) $\mu = 0, \phi = \pi/6$, nontrivial semi-metallic phase with pseudo-gap, (c) $\mu/t_1 = 1, \phi = 0$, trivial semi-metallic phase with band-gap point shifting to K' point, (d) $\mu/t_1 = 1.5, \phi = 0$, trivial insulating phase with true band gap, (e) $\mu/t_1 = 0.5, \phi = \pi/6$, Chern semimetallic phase with $C_n = (-1, 1)$, (f) $\mu/t_1 = 0.5, \phi = -\pi/6$, Chern semimetallic phase with $C_n = (1, -1)$

IV. TOPOLOGICAL PROPERTIES

A. Chern numbers and Hall conductivity

As pointed out before, nontrivial topological phases are characterized by the value of topological invariant, C which can assume only integral value as it belongs to 2D symmetry class A⁴¹. So, for both CI and CSM phases, each energy band is characterized by band Chern number, C_n , where n is the band index. Again, over all the bands, $\sum_n C_n = 0$, and some of the bands must have nonzero C_n for the system to be nontrivial. However, for the two-band topological system, each band must have nonzero value of C_n , but opposite in sign. In this section, value of C_n has been determined in order to characterize the topological phases of this system. C_n is defined as the integration of the Berry curvature $\Omega_n(\mathbf{k})$ over the first BZ (1BZ), *i.e.*,

$$C_n = \frac{1}{2\pi} \int_{1\text{BZ}} d^2\mathbf{k} \cdot \Omega_n(\mathbf{k}), \quad (4)$$

where $\Omega_n(\mathbf{k}) = -i(\langle \partial_1 u_{n,\mathbf{k}} | \partial_2 u_{n,\mathbf{k}} \rangle - \langle \partial_2 u_{n,\mathbf{k}} | \partial_1 u_{n,\mathbf{k}} \rangle)$. Here $|u_{n,\mathbf{k}}\rangle$ are the eigenvectors for the n -th band of $h(\mathbf{k})$ and $\partial_i = \frac{\partial}{\partial k_i}$. C_n is well-defined for a particular band as long as it does not touch other neighbouring bands *i.e.*, there exists true or pseudo-gap between the bands. Chern metallic (CM) phase has also been reported before, where bands overlap each other¹⁶, but in that case Chern number C_n is not defined and the bands are characterized by Hall conductance. In our numerical calculation, we use the discretized version of Eq. 4 introduced by Fukui and others in order to determine C_n ⁴².

In this model, the presence of TRS breaking NNNN phase, ϕ and sublattice symmetry breaking term μ gives rise to the non-vanishing Chern numbers. The system is in nontrivial phase for the entire range $-1 < \mu/t_1 < 1$, and $-\pi \leq \phi \leq \pi$, except at $\phi = 0$. As soon as $|\mu|/t_1 = 1$, transition occurs from nontrivial to trivial phase, and the Chern numbers of the bands become zero. For $\phi < 0$ ($\phi > 0$), the Chern numbers are $C = (1, -1)$ ($C = (-1, 1)$). So, whenever the value of ϕ crosses the $\phi = 0$ line for $-1 < \mu/t_1 < 1$, phase transition occurs from $C = (-1, 1)$ to $C = (1, -1)$ which is accompanied by closing and reopening of the band gap.

However, Chern numbers for this 2D two-band system can be obtained analytically using the generalized formula⁴³,

$$C_n = \frac{1}{2} \sum_{\mathbf{k} \in D_j} \text{sgn}(J(\mathbf{k})_z) \cdot \text{sgn}(h(\mathbf{k})_z), \quad (5)$$

where $\mathbf{J}(\mathbf{k}) = (\partial_{k_x} \mathbf{h}(\mathbf{k})) \times (\partial_{k_y} \mathbf{h}(\mathbf{k}))$, and D_j 's are the Dirac points for the Hamiltonian. Dirac point corresponds to the location in the BZ where doubly degenerate states exist. In this case, by choosing $h(\mathbf{k})_z$ as the arbitrary axis, Dirac points are obtained by setting $h(\mathbf{k})_x = 0$, and $h(\mathbf{k})_y = 0$. At this moment, locations of Dirac points are obtained by the solutions of the equation, $h(\mathbf{k})_z = 0$. Thus the coordinates of the Dirac points are given by $D_1 = (0, \pi)$, and $D_2 = (\pi, \pi)$ for $\phi \neq 0$, those are nothing but the high-symmetry points in BZ, K' and M , respectively. Now $\text{sgn}(J_z(\mathbf{k}))$ and $\text{sgn}(h_z(\mathbf{k}))$ in the parameter space can be obtained in a simple way which are given in the following table when $t_2/t_1 = 1$, and $t_3/t_1 = 1/2$.

| Conditions | $[\text{sgn}(h_z) \cdot \text{sgn}(J_z)]_{D_1}$ | $[\text{sgn}(h_z) \cdot \text{sgn}(J_z)]_{D_2}$ | C_n |
|--|---|---|-------|
| $-1 < \mu/t_1 < 1,$ $0 < \phi < \pi$ | $1 \cdot 1 = 1$ | $(-1) \cdot (-1) = 1$ | 1 |
| $\mu/t_1 < -1,$ $0 < \phi < \pi$ | $1 \cdot 1 = 1$ | $1 \cdot (-1) = -1$ | 0 |
| $\mu/t_1 > 1,$ $0 < \phi < \pi$ | $(-1) \cdot 1 = -1$ | $(-1) \cdot (-1) = 1$ | 0 |
| $-1 < \mu/t_1 < 1,$ $-\pi < \phi < 0$ | $1 \cdot (-1) = -1$ | $(-1) \cdot 1 = -1$ | -1 |
| $\mu/t_1 < -1,$ $-\pi < \phi < 0$ | $1 \cdot (-1) = -1$ | $1 \cdot 1 = 1$ | 0 |
| $\mu/t_1 > 1,$ $-\pi < \phi < 0$ | $(-1) \cdot (-1) = 1$ | $(-1) \cdot 1 = -1$ | 0 |

TABLE I: Chern number in different parameter regime using the Eq. 5.

Afterwards it is straightforward to check that in the parameter regime: $-1 < \mu/t_1 < 1$, $\phi = \pi/6$, the value of Chern number, $C_n = \frac{1}{2}(1+1) = 1$, and for the parameter regime: $|\mu|/t_1 > 1$, $\phi = \pi/6$, the value of Chern number, $C_n = \frac{1}{2}(-1+1) = 0$, and so on. Evidently, the result matches with the numerically calculated values as obtained before. Therefore, the system undergoes phase transitions at the points, $\mu/t_1 = \pm 1$, for any nonzero values of ϕ , where the transition takes place between nontrivial and trivial phases. Another transition between two nontrivial phases occurs around the point $\phi = 0$, irrespective of any values of the remaining parameters. Band gap vanishes at every transition point. Obviously coordinates of D_j 's depend on the values of parameters.

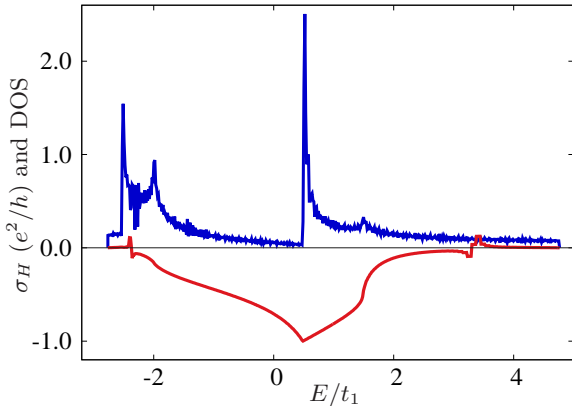


FIG. 4: The Hall conductance σ_H (red line) and DOS (blue line) with respect to the Fermi energy E for $t_2/t_1 = 1$, $t_3/t_1 = 1/2$, $\mu/t_1 = 1/2$, $\phi = \pi/6$. σ_H shows a sharp edge instead of a plateau due to semimetallic phase. It indicates the absence of true band gap.

The Hall-conductivity ($\sigma_H(E)$) is another important quantity for determining topological phase since it can be verified experimentally. At zero temperature, $\sigma_H(E)$ for this system has been estimated numerically

by using the Kubo formula²,

$$\sigma_H(E) = \frac{ie^2\hbar}{A_0} \sum_{E_m < E < E_n} \frac{\langle m|v_x|n\rangle\langle n|v_y|m\rangle - \langle m|v_y|n\rangle\langle n|v_x|m\rangle}{(E_m - E_n)^2}, \quad (6)$$

where $|l\rangle = |u_{l,\mathbf{k}}\rangle$, $h_{\mathbf{k}}|l\rangle = E_l|l\rangle$, and $l = m, n$. A_0 is the area of the system and E is the Fermi energy, while e is the charge of electron. The velocity operator, $v_\alpha = (1/i\hbar)[\alpha, H]$, where $\alpha = x, y$. When E falls in one of the energy gaps, the contribution to σ_H by the completely filled bands is given by

$$\sigma_H(E) = \frac{e^2}{h} \sum_{E_n < E} C_n. \quad (7)$$

The value of $\sigma_H(E)$ over any Hall plateau becomes equal to the sum of all Chern numbers carried by the bands having energy lower than it. The Hall-conductivity shows quantized plateau as long as Fermi energy lies in the band-gap. The height of the plateau is determined by the Chern number of respective bands according to equation 7. Variations of $\sigma_H(E)$ and DOS for the monolayer depleted Lieb lattice with respect to Fermi energy, E are shown in Fig 4. As shown in Fig 4, the height of the plateau is $\sigma_H = n(e^2/h)$, with $n = -1$ since the Chern number distribution is $C_n = (-1, 1)$. The width of the plateau tends to zero since the phase is always semimetallic. $\sigma_H(E)$ shown in Fig 4 mostly assumes negative values due to the topological phase $C_n = (-1, 1)$. Obviously it will be opposite if it is drawn for the other topological phase $C_n = (1, -1)$.

B. Topological Edge States

'Bulk boundary correspondence' rule states that the sum of Chern numbers up to the i -th band,

$$\nu_i = \sum_{j \leq i} C_j, \quad (8)$$

is equal to the number of pair of edge states in the gap⁴⁴. In order to establish this relation, a 1D ribbon of depleted Lieb lattice is created by removing the periodic boundary condition (PBC) along y direction so that k_y is no longer a good quantum number. We consider $N = 200$ sites along y -direction and diagonalize the resulting Hamiltonian as a function of good quantum number k_x , since the PBC along x -direction is present.

In Fig 5, the energy eigen-values are plotted for $t_2/t_1 = 1$, $t_3/t_1 = 1/2$, $\mu/t_1 = 1/2$, $\phi = \pi/6$. Evidently, one pair of edge modes exists in the band gap according to bulk-boundary rule since the Chern numbers are $(-1, 1)$ in ascending order of energy. Two edge modes connect the two bands but in opposite direction. The edge states are always localized in the left edge (orange curves) or right edge (skyblue curves) as verified from the lower panel of Fig 5. Edge states are chiral in nature since the states with positive (negative) group velocity are localized in the right (left) edge. The side

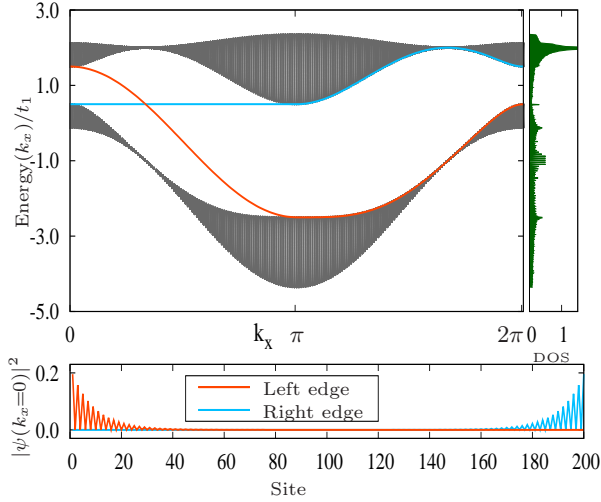


FIG. 5: Edge states of depleted Lieb lattice for the parameters $t_2/t_1 = 1$, $t_3/t_1 = 1/2$, $\mu/t_1 = 1/2$, $\phi = 2\pi/3$ for $N = 200$ unit cells along y direction. Chern numbers of the bands are $C_n = -1, 1$. The side-panel indicates the density of states. Lower panel shows the distribution of probability density of left (orange) and right (skyblue) going edge states with respect to site number of the strip for $k_x = 0$.

panel shows the value of density of states (DOS) of the system with ribbon geometry, which clearly indicates the absence of true (direct) band gap for those particular parameters. Tight-binding model identical to the original Haldane model, comprising complex NNN term and absence of NNNN hopping could not lead to nontrivial topology for the depleted Lieb lattice.

V. BILAYER DEPLETED LIEB LATTICE

A. Formulation of Hamiltonian

In this section, a system for coupled bilayer of depleted Lieb lattice is considered, where two monolayer lattice is stacked identically. So, the A (B) sublattice of the bottom layer lies exactly below the A (B) sublattice of the top layer. Structure of bilayer depleted Lieb lattice is shown in Fig 1 (c). Similar to the monolayer model, the tight binding Hamiltonian is formulated in the following manner,

$$\begin{aligned}
 H = & \sum_{q \in t, b} \left[t_1 \sum_{\langle jj' \rangle} c_j^{q\dagger} c_{j'}^q + t_2 \sum_{\langle\langle jj' \rangle\rangle \in A} c_j^{q\dagger} c_{j'}^q \right. \\
 & + t_3 \sum_{\langle\langle\langle jj' \rangle\rangle} e^{i\phi_{jj'}^q} c_j^{q\dagger} c_{j'}^q + H.c \left. \right] + t_4 \left[\sum_j c_j^{t\dagger} c_j^b + H.c \right] \\
 & + \sum_{j, q \in t, b} \mu_j c_j^{q\dagger} c_j^q. \quad (9)
 \end{aligned}$$

where q indicates the layer index, which can be 't' (top layer) or 'b' (bottom layer). $c_j^{q\dagger}$ (c_j^q), $q \in t, b$, is the fermionic creation (annihilation) operator for an electron at the j -th site at top (t) or bottom (b) layer. t_1, t_2

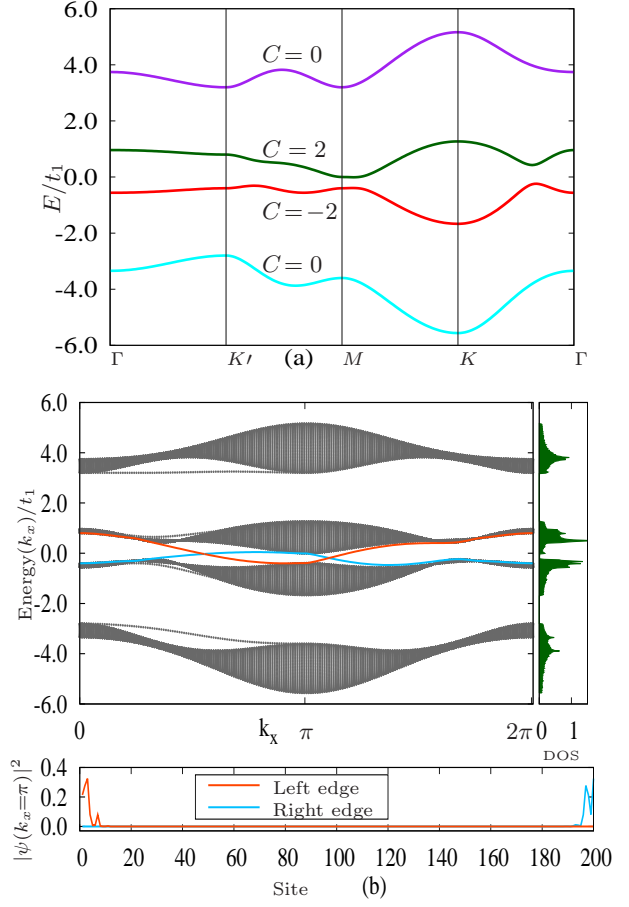


FIG. 6: (a) Band structure along the high symmetry points of BZ for the bilayer depleted Lieb lattice when $t_2/t_1 = 0.2$, $t_3/t_1 = 0.5$, $t_4/t_1 = 1.8$, $\mu/t_1 = 1.4$, $\phi^b = 2.8$, $\phi^t = 1.6$. (b) Edge states of the bilayer depleted Lieb lattice ribbon for the same parameters for $N = 200$ unit cell along y direction. Chern numbers of the bands are $C_n = (0, -2, 2, 0)$. The side-panel indicates the DOS of the ribbon. Lower panel shows the distribution of probability density of left (orange) and right (skyblue) going edge states with respect to site number of the strip for $k_x = \pi$.

and t_3 is the strength of NN, NNN and NNNN hopping respectively and these are same for both the layers. t_4 is the strength of inter-layer hopping between A (and B) sublattices of both the layer. The direction of the phases $\phi_{jj'}$ is same as in monolayer case, while ϕ^t and ϕ^b can be different. However, choice of directions conforms to the fact that total field crossing the square plaquette is again zero. The onsite energy is taken as $\mu_B = -\mu_A = \mu$, for both the layers. None other than NN hopping between the two layers is taken into account.

Using PBC along both x and y directions, the Hamiltonian can be written in the momentum space:

$$H = \sum_{\mathbf{k}} \psi_{\mathbf{k}}^\dagger h(\mathbf{k}) \psi_{\mathbf{k}}, \quad (10)$$

where $\psi_{\mathbf{k}}^\dagger = [c_{A\mathbf{k}}^{t\dagger} c_{B\mathbf{k}}^{t\dagger} c_{A\mathbf{k}}^{b\dagger} c_{B\mathbf{k}}^{b\dagger}]$, is a four-component spinor and $h(\mathbf{k})$ is a 4×4 matrix. The upper diag-

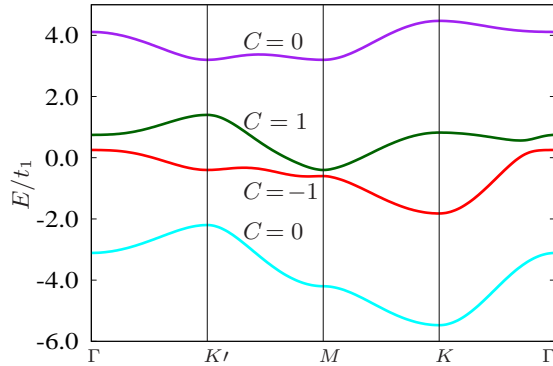


FIG. 7: Band structure along the high symmetry points of BZ for the bilayer depleted Lieb lattice when $t_2/t_1 = 0.5$, $t_3/t_1 = 0.25$, $t_4/t_1 = 1.8$, $\mu/t_1 = 1.4$, $\phi^b = 2.8$, $\phi^t = 1.6$. Chern numbers of the bands from the top are $C_n = (0, 1, -1, 0)$.

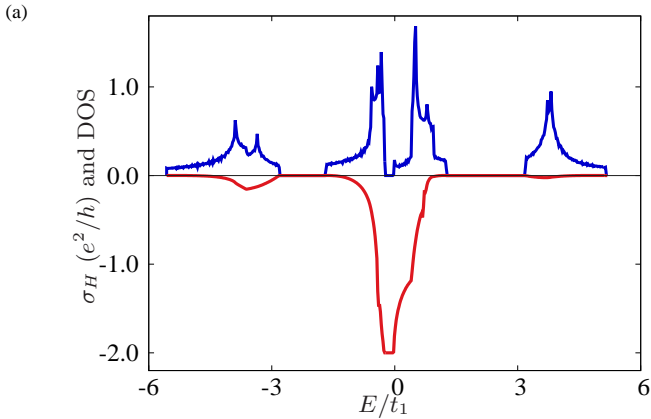


FIG. 8: The Hall conductance σ_H (red line) and DOS (blue line) with respect to the Fermi energy, E for bilayer depleted Lieb lattice when $t_2/t_1 = 0.2$, $t_3/t_1 = 0.5$, $t_4/t_1 = 1.8$, $\mu/t_1 = 1.4$, $\phi^t = 2.8$, $\phi^b = 1.6$. σ_H shows three plateaus where DOS vanishes.

onal components of $h(\mathbf{k})$ are given by

$$\begin{aligned}
 h_{11} &= -\mu + 2t_2 \cos(k_x) = h_{33}, \\
 h_{12} &= 2t_1 \cos\left(\frac{k_y}{2}\right) + 4t_3 \cos(\phi^b) \cos(k_x) \cos\left(\frac{k_y}{2}\right) \\
 &\quad - 4it_3 \sin(\phi^b) \sin(k_x) \sin\left(\frac{k_y}{2}\right), \\
 h_{13} &= t_4 = h_{24}, \\
 h_{22} &= \mu = h_{44}, \\
 h_{34} &= 2t_1 \cos\left(\frac{k_y}{2}\right) + 4t_3 \cos(\phi^t) \cos(k_x) \cos\left(\frac{k_y}{2}\right) \\
 &\quad - 4it_3 \sin(\phi^t) \sin(k_x) \sin\left(\frac{k_y}{2}\right).
 \end{aligned} \tag{11}$$

The other components are zero and the lower diagonal components are complex conjugate of the upper diagonal components. Diagonalizing this matrix numerically, we obtain the band spectrum. In the large parameter-space, there is very few region where the sys-

tem is in a insulating or semi-metallic phase. In most of the region, the system is in metallic phase. One of the nontrivial insulating phase is shown in Fig 6 (a), in which the middle bands carry nonzero Chern numbers. Similarly, one nontrivial semimetallic phase has been identified as shown in Fig 7. No inversion symmetry about $E = 0$ is found in those band structures which means PHS is absent in this bilayer model like the monolayer one.

B. Topological Properties

Following equation 4 and the numerical method developed by Fukui and others, we calculate the Chern numbers of the band. Nonzero Chern numbers are obtained for the values $t_2/t_1 = 0.2$, $t_3/t_1 = 0.5$, $t_4/t_1 = 1.8$, $\mu/t_1 = 1.4$, $\phi^b = 2.8$, $\phi^t = 1.6$. In ascending order of energy, the Chern numbers are given by $C_n = (0, -2, 2, 0)$. Hence, the system is in the CI phase for this particular set of values. Another CI phase with $C_n = (0, 2, -2, 0)$ is obtained by reversing the signs of ϕ^b and ϕ^t , simultaneously. It is interesting to note that, higher Chern number is obtained by coupling two identical layers of depleted Lieb lattice. If we vary the parameters, the middle two bands overlap and the Chern number becomes undefined. In addition, one pair of CSM phases with $C_n = (0, \mp 1, \pm 1, 0)$ have been identified when $t_2/t_1 = 0.5$, $t_3/t_1 = 0.25$, $t_4/t_1 = 1.8$, $\mu/t_1 = 1.4$, $\phi^b = \pm 2.8$, $\phi^t = \pm 1.6$. So unlike the monolayer system, both CI and CSM phases are found in the bilayer system.

In order to check the ‘bulk boundary correspondence’ rule, two isolated edges are created by means of bilayer depleted Lieb lattice ribbon for the system. The effective Hamiltonian is obtained by removing the PBC along y direction. In order to get the edge states, system of $N = 200$ sites along y direction is considered and the resulting Hamiltonian is diagonalized where energies obtained as a function of good quantum number k_x . In Fig 6 (b), the energy eigen-values are plotted for the particular set of values. In this occasion, two pairs of in-gap edge modes are found to exist since the middle two bands carry the Chern numbers, either $C_n = \pm 2$, or $C_n = \mp 2$, depending on the sign of ϕ 's. The chiral and localized nature of edge states are also verified from the plot. The side-panel shows the DOS of the ribbon which reveals the existence of true band gap. Variations of $\sigma_H(E)$ and DOS for the bilayer depleted Lieb lattice with respect to Fermi energy, E are shown in Fig 8, when $t_2/t_1 = 0.2$, $t_3/t_1 = 0.5$, $t_4/t_1 = 1.8$, $\mu/t_1 = 1.4$, $\phi^t = 2.8$, $\phi^b = 1.6$. Hall conductivity shows three plateaus where DOS vanishes. Two plateaus are found when $\sigma_H(E) = 0$, and one at $\sigma_H(E) = -2$. In contrast no plateau is found for the monolayer system, since true band gap is absent there. The width of the plateau depends on the width of the band gap. As shown in Fig 8, the height of the plateau is $\sigma_H = n(e^2/h)$, with $n = -2$ since the Chern number distribution is $C_n = (-2, 2)$.

VI. SUMMARY AND DISCUSSIONS

Search of topological phases in various materials became an intriguing part of investigation in condensed matter physics. Theoretical discovery of QAHE leads to an enormous possibility of finding new topological phases in a variety of systems in the absence of true magnetic field³. Investigations in this field began by formulating theoretical models on specific lattice structures. In the 2D systems, nontrivial topological phases are found to exist on the models formulated on non-Bravais lattices. Symmetries of studied models reveal that those non-Bravais lattices can be derived from either square or triangular lattices. For examples, Lieb¹², CaVO^{25,27,28}, square-octagon^{13,19} and checkerboard¹⁶ lattices are derived from square lattice, while honeycomb³, stuffed-honeycomb¹⁵, kagome^{13,14}, breathing kagome⁷, star^{17,18}, α - \mathcal{T}_3 ¹⁰ and dice¹¹ are derived from triangular lattice. Investigation in this field continues thereafter by means of finding topological phase on remaining non-Bravais lattices.

Previous study on the monolayer depleted Lieb lattice predicted no topological phase while formulating FM XXZ Heisenberg model with NN, NNN and NNNN exchange interactions even in the presence of DM term and external magnetic field³⁹. In contrast, this study lets out the existence of nontrivial topological phases in monolayer and bilayer structures of depleted Lieb lattice. This 2D non-Bravais lattice is generated out of square lattice by removing its sites systematically in such a way that four-fold rotational symmetry of original square lattice reduces to two-fold. The resulting

monolayer lattice is bipartite while the bilayer lattice is quadripartite.

In the nontrivial regime, each of the models host two topological phases. In each case, tight-binding models are formulated incorporating NN, NNN and NNNN hopping terms where NNNN terms are complex. The phases of the complex terms is chosen in such a way that net magnetic field per square plaquette vanishes. Although, model with this characteristic feature does hold topologically nontrivial phase, additional staggered onsite energy term is taken into account in order to note another transition from nontrivial to trivial phase. System undergoes two types of phase transitions, namely, between two nontrivial phases and nontrivial to trivial phases. Topological phases found in monolayer model are characterized by $C_n = (\pm 1, \mp 1)$, while those for bilayer model are defined by $C_n = (0, \pm 2, \mp 2, 0)$, and $C_n = (0, \mp 1, \pm 1, 0)$. CSM phase appears in monolayer model while both CI and CSM phases emerge in bilayer case as they are noted before. Also as stated before tight-binding model on depleted Lieb lattice identical to the original Haldane model could not lead to nontriviality. It is now established that any artificial 2D lattices can be realized by means of photonic and cold-atom crystals or by synthesizing the surface state electrons on Cu(111)/CO substrate³⁷. Existence of edge states may be verified in this route. Detection of topological phase is also possible by observing the feature of $\sigma_H(E)$, if real materials is found in future. At the same time, search of new topological phases in the remaining non-Bravais lattices will be carried on.

-
- * Electronic address: arghyasil36@gmail.com
 † Electronic address: asinkumar96@yahoo.com
- ¹ Klitzing K. V., Rev. Mod. Phys. **58**, 519 (1986).
 - ² Thouless D. J., Kohomoto M., Nightingale P. and den Nijs M., Phys. Rev. Lett. **49**, 405 (1982).
 - ³ Haldane F. D. M., Phys. Rev. Lett. **61**, 2015 (1988).
 - ⁴ Y. Hatsugai, Phys. Rev. Lett. **71**, 3697 (1993).
 - ⁵ Benalcazar W. A., Bernevig B. A., and Hughes T. L., Science **357**, 61 (2017).
 - ⁶ Benalcazar W. A., Bernevig B. A., and Hughes T. L., Phys. Rev. B **96**, 245115 (2017).
 - ⁷ Sil A. and Ghosh A. K., J. Phys.: Condens. Matter **32**, 205601 (2020).
 - ⁸ Alba E., Gonzalvo X. F., Petit J. M., Pachos J. K., and Ripoll J. J. G, Phys. Rev. Lett. **107**, 235301 (2011)
 - ⁹ Shao L. B., Zhu S. L., Sheng L., Xing D. Y., and Wang Z. D., Phys. Rev. Lett. **101**, 246810 (2008)
 - ¹⁰ B Dey and T K Ghosh, Phys. Rev. B **99** 205429 (2019).
 - ¹¹ Mondal S. and Basu S. Phys. Rev. B **107** 035421 (2023).
 - ¹² Weeks C and Franz M 2010 Phys. Rev. B **82** 085310.
 - ¹³ Liu X P, Chen W C, Wang Y F and Gong C D 2013 J. Phys.:Condens. Matter **25** 305602
 - ¹⁴ Guo H. M. and Franz M., Phys. Rev. B **80**, 113102 (2009).
 - ¹⁵ Sil A. and Ghosh A. K., J. Phys.: Condens. Matter **32**, 025601 (2019).
 - ¹⁶ Sun K, Gu Z, Katsura H and Das Sarma S 2011 Phys. Rev. Lett. **106** 236803.
 - ¹⁷ Chen W C, Liu R, Wang Y F and Gong C D 2012 Phys. Rev. B **86** 085311 (2012).
 - ¹⁸ M Chen and S Wan, J. Phys.: Condens. Matter **24**, 325502 (2012).
 - ¹⁹ Kargarian M and Fiete G A 2010 Phys. Rev. B **82** 085106.
 - ²⁰ Hasan M. Z. and Kane C. L., Rev. Mod. Phys. **82**, 3045 (2010).
 - ²¹ Oka T and Aoki H 2009 Phys. Rev. B **79** 081406.
 - ²² Sil A. and Ghosh A. K., J. Phys.: Condens. Matter **31**, 245601 (2019).
 - ²³ Owerre S A 2017 Phys. Rev. B **95** 014422.
 - ²⁴ M Deb and A K Ghosh, J. Phys.: Condens. Matter **31**, 345601 (2019).
 - ²⁵ M Deb and A K Ghosh, J. Magn. Magn. Mater. **533** 167968 (2021)
 - ²⁶ M Deb and A K Ghosh, J. Phys.: Condens. Matter **32**, 365601 (2020).
 - ²⁷ M Deb and A K Ghosh, Eur. Phys. J. B **93**, 145 (2020).
 - ²⁸ I Bose and A Ghosh, Phys. Rev. B **56** 3149 (1997).
 - ²⁹ Owerre S A 2017 Phys. Rev. B **94** 094405.
 - ³⁰ Sorn S., Phys. Rev. B **98**, 125145 (2018).
 - ³¹ Nita M., Ostahie B., and Aldea A., Phys. Rev. B **82**, 125428 (2013).
 - ³² Beugeling W., Everts J. C. and Smith C. M., Phys. Rev. B **86**, 195129 (2012).

- ³³ Karnaukhov I. N. and Sleptsov I. O., (arXiv:1510.07239v1) (2015).
- ³⁴ Long Y. and Ren J., (arXiv:1706.01107) (2017).
- ³⁵ X. Cao, K. Chen and D. He, J. Phys.: Condens. Matter **27**, 166003 (2015).
- ³⁶ Banerjee S. and Saxena A., Phys. Rev. B **103**, 235125 (2021).
- ³⁷ Slot M. *et al.*, Nature Phys **13**, 672-676 (2017).
- ³⁸ B Cui *et al.*, Nat. Commun. **11**, 66 (2020).
- ³⁹ de Oliveira P. G. and Pires A.S.T., Physica B **654**, 414721(2023).
- ⁴⁰ Kambe S. and Ishii, Physica C 341-348 (2000) 555-556.
- ⁴¹ S. Ryu, A. P. Schnyder, A. Furusaki, and A. W. W. Ludwig, New J. Phys., **12** 065010 (2010).
- ⁴² Fukui T., Hatsugai Y. and Suzuki H., J. Phys. Soc. Jpn. **74**, 1674 (2005).
- ⁴³ D. Sticlet, F. Piéchon, J.-N. Fuchs, P. Kalugin, and P. Simon, Phys. Rev. B **85**, 165456 (2012).
- ⁴⁴ A. Mook, J. Henk and I. Mertig, Phys. Rev. B **90**, 024412 (2014).